Journal of Biomedical Optics 11(2), 024014 (March/April 2006)

Doppler flow imaging of cytoplasmic streaming using spectral domain phase microscopy

Michael A. Choma
Audrey K. Ellerbee
Siavash Yazdanfar*
Joseph A. Izatt
Duke University
Department of Biomedical Engineering
Durham, North Carolina 27708
E-mail: mac32@duke.edu

Abstract. Spectral domain phase microscopy (SDPM) is a function extension of spectral domain optical coherence tomography. SDPM achieves exquisite levels of phase stability by employing common-path interferometry. We discuss the theory and limitations of Doppler flow imaging using SDPM, demonstrate monitoring the thermal contraction of a glass sample with nanometer per second velocity sensitivity, and apply this technique to measurement of cytoplasmic streaming in an *Amoeba proteus* pseudopod. We observe reversal of cytoplasmic flow induced by extracellular $CaCl_2$, and report results that suggest parabolic flow of cytoplasm in the *A. proteus* pseudopod.
[DOI: 10.1117/1.2193167]

Keywords: optical coherence tomography; doppler; microscopy; cytoplasm; interference microscopy; noise in imaging systems.

Paper 05102RR received Apr. 19, 2005; revised manuscript received Nov. 13, 2005; accepted for publication Nov. 14, 2005;

1 Introduction

Doppler flow imaging was one of the first functional extensions developed for optical coherence tomography,[1,2] (OCT) There are two important aspects of OCT that enable phase imaging, in general, and Doppler flow imaging, in particular. First, since OCT is interferometric in nature, light that is Doppler shifted by the motion of scattering particles within the sample creates an electronic beat frequency proportional to the axial component of the sample particle velocity. Second, since OCT performs depth ranging with a broadband light source, this beat frequency can be recorded as a function of sample depth, which enables the generation of depth-indexed flow profiles.

Because Doppler flow imaging in OCT requires phase sensitive detection, interferometric phase stability is critical. Time domain (TD) and spectral domain (SD) systems have different considerations for phase stability. TD-OCT systems employ a broadband light source, a scanning delay line, and a single photodiode detector. As the group delay between the reference and sample arms is scanned, the interferometric signal generated is proportional to the sample reflectivity at the sample depth corresponding to the instantaneous group delay. As such, the phase stability in TD-OCT is limited by the linearity and repeatability of the reference arm group delay scan. SD-OCT systems employ a stationary reference arm and simultaneously collect light from all depths in the sample by collecting the interference signal as a function of optical wavelength. This spectrally indexed signal is Fourier transformed to calculate the depth-indexed sample reflectivity profile (i.e., A scan). The spectral interferometric signal is collected by either (1) using a broadband source and a spectrometer in the detector arm (Fourier domain OCT) or (2) measuring with a single photodiode the signal generated by sweeping a narrow-linewidth laser source through a broad bandwidth (swept source OCT). In SD-OCT systems employing a Michelson interferometer, the phase stability is limited by jitter in the relative path lengths between the sample and reference arms, and in the case of swept source OCT, the repeatability of the wavelength sweep. Indeed, it has been demonstrated that SD-OCT is more stable than its TD counterpart.[3]

Recently, several phase-sensitive extensions of OCT have been demonstrated.[1,2,4–9] Recently, we demonstrated SD phase microscopy (SDPM), a functional extension of OCT that employs common path SD interferometry[10,11] to achieve phase stabilities in the milliradian regime.[12] In this paper, we use SDPM to perform Doppler flow imaging of cytoplasmic streaming in an *Amoeba proteus*, which is very mobile unicellular protozoan that has been widely used for decades to study the mechanisms of cytoplasm physiology and cell motility.[13–18] Cytoplasmic streaming is an important cellular process that plays a role in events ranging from metastasis in cancer to cellular locomotion to cell division. We derive an expression for the shot-noise-limited flow velocity resolution of SDPM, and compare the performance of our system to this theoretical limit.

2 Phase-Resolved SD Interference Signal

The SD photocurrent in SD-OCT and SDPM is given by[19]

$$i(k)=\frac{1}{2}\rho S(k)\,\delta k\left\{R_R+\sum_n R_n + 2\sqrt{R_R}\sum_n\sqrt{R_n}\cos[2k(\Delta x_n+\delta x_n)]\right\}. \quad (1)$$

Here, $S(k)$ is the source power spectral density, k is the wave

---

*Current affiliation: GE Global Research, Applied Optics Lab, Niskayuna, New York 12309.

Address all correspondence to Michael Choma, Biomedical Engineering, Duke University, 136 Hudson Hall — Box 90281, Durham, NC 27708. Tel: 919–660–2475. Fax: 919–613–9144. E-mail: mac32@duke.edu

1083-3668/2006/11(2)/024014/8/$22.00 © 2006 SPIE

number (radians per meter), δk is the spectral channel bandwidth, ρ is the detector responsivity, R_R is the reference arm reflectivity, and R_n is the reflectivity of the n'th sample reflector. The quantity $\Delta x_n+\delta x_n$ is the position of the n'th reflector; Δx_n is an integer multiple of the discrete sampling interval in the x domain, given by $m\pi/\Delta k$, where Δk is the total optical bandwidth interrogated and m is any positive or negative integer; and δx_n accounts for subresolution deviations in reflector position away from $m\pi/\Delta k$. Note that δx_n is an important quantity because it primarily manifests in the phase of $i(k)$. Note also that n and m are distinct and separate variables: n indexes discrete reflectors in the sample, while m indexes elements in the 1-D x domain A scan array.

In swept source OCT $i(k)$ is directly measured, whereas in spectrometer-based Fourier domain OCT, $i(k)$ is integrated over the A scan acquisition time in a charge-coupled device (CCD) or similar charge-accumulation detector. In either case, after Fourier transformation of the k domain signal, the complex-valued x domain signal and shot noise are given by, respectively,

$$\mathbf{I}_{\text{signal}}(2\Delta x_n)=\frac{\rho S_0(R_R R_n)^{1/2}}{2ef_{\text{ascan}}}E(2\delta x_n)\exp(jk_0 2\delta x_n), \tag{2}$$

$$\mathbf{I}_{\text{noise}}(2\Delta x_n)=\left(\frac{\rho S_0 R_R}{ef_{\text{ascan}}}\right)^{1/2}\exp(j\phi_{\text{rand}}). \tag{3}$$

Here, $E(\cdot)$ is the unity-amplitude x domain autocorrelation function, S_0 is the total sample illumination power [i.e., $\int S(k)\,\mathrm{d}k$], k_0 is the source center wavenumber, ϕ_{rand} is the random phase of the shot noise, and f_{ascan} is the rate in hertz at which A scans were acquired. In situations where the detector integration time is less than the interval between acquired A scans, f_{ascan} is the numerical inverse of the integration time. It is assumed that $R_R \gg R_n$. The amplitude signal to noise ratio of the n'th reflector is given by the square of the ratio of the amplitudes of Eqs. (2) and (3). The shot-noise-limited phase stability of the n'th reflector signal is limited by the phase angle $\delta\phi_{\text{sens}}$ between $\mathbf{I}_{\text{signal}}(2\Delta x_n)$ and $\mathbf{I}(2\Delta x_n)=\mathbf{I}_{\text{signal}}(2\Delta x_n)+\mathbf{I}_{\text{noise}}(2\Delta x_n)$. In our previous work,[12] we derived an expression for $\delta\phi_{\text{sens}}$ by considering its upper limit when $\mathbf{I}_{\text{signal}}$ and $\mathbf{I}_{\text{noise}}$ are orthogonal (i.e., $\phi_{\text{rand}}=2k_0\delta x_n \pm \pi/2$). The issue can be more generally approached by considering the average value of the phase angle between $\mathbf{I}_{\text{signal}}(2\Delta x_n)$ and $\mathbf{I}(2\Delta x_n)$ over all values of ϕ_{rand}. This is given by (Fig. 1):

$$\delta\phi_{\text{sens}}=\frac{2}{\pi}\int_0^{\pi/2}\tan^{-1}\left(\frac{|\mathbf{I}_{\text{noise}}|}{|\mathbf{I}_{\text{signal}}|}\sin\phi_{\text{rand}}\right)\mathrm{d}\phi_{\text{rand}}. \tag{4}$$

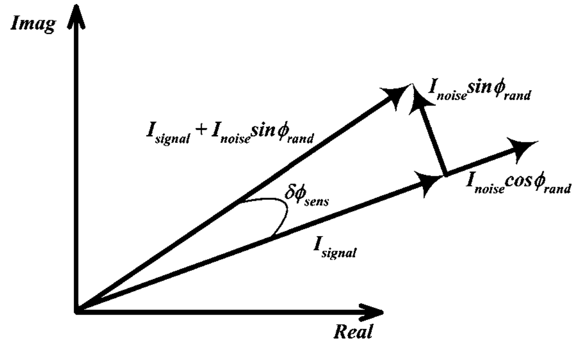

Fig. 1 Phase stability of spectral domain phase microscopy. In the x domain the signal and noise are complex-valued signals that add in a vectoral manner. If the phase of the noise is defined to be zero when $\mathbf{I}_{\text{noise}}$ is parallel to $\mathbf{I}_{\text{signal}}$, then the error in the phase of $\mathbf{I}_{\text{signal}}$ is given by the component of $\mathbf{I}_{\text{noise}}$ that is perpendicular to $\mathbf{I}_{\text{signal}}$ (i.e., $\mathbf{I}_{\text{noise}}\sin\phi_{\text{rand}}$). The average rotation of $\mathbf{I}_{\text{signal}}$ caused by $\mathbf{I}_{\text{noise}}\sin\phi_{\text{rand}}$ taken over all ϕ_{rand} defines the phase stability.

Equation (4) is derived in part from the representation of signal and noise in Fig. 1. At any particular instant, the signal vector ($\mathbf{I}_{\text{signal}}$) and the noise vector ($\mathbf{I}_{\text{noise}}$) have a random angular orientation with respect to each other. Since the phase of $\mathbf{I}_{\text{signal}}$ is not random, the phase of $\mathbf{I}_{\text{noise}}$ (i.e., ϕ_{rand}) can be conveniently defined with respect to $\mathbf{I}_{\text{signal}}$, and $\mathbf{I}_{\text{noise}}$ can be decomposed into components that are parallel ($\mathbf{I}_{\text{noise}}\cos\phi_{\text{rand}}$) and orthogonal ($\mathbf{I}_{\text{noise}}\sin\phi_{\text{rand}}$) to the signal vector. The parallel component contributes to amplitude sensitivity, while the orthogonal component contributes to the phase sensitivity. The phase noise of $\mathbf{I}_{\text{signal}}$ is defined by the magnitude of the rotation of $\mathbf{I}_{\text{signal}}$ by $\mathbf{I}_{\text{noise}}\sin\phi_{\text{rand}}$. The phase noise also defines the phase sensitivity ($\delta\phi_{\text{sens}}$) since the smallest observable change in the phase of the signal vector is determined by the phase noise. In other words, an observable change in the signal phase must be larger than the phase noise. If $|\mathbf{I}_{\text{noise}}| \ll |\mathbf{I}_{\text{signal}}|$, which is the usual case, then $\mathbf{I}_{\text{signal}}$, $\mathbf{I}_{\text{noise}}\sin\phi_{\text{rand}}$, and $\mathbf{I}_{\text{signal}}+\mathbf{I}_{\text{noise}}\sin\phi_{\text{rand}}$ form a right triangle, and $\delta\phi_{\text{sens}}$ is the angle opposite $\mathbf{I}_{\text{noise}}\sin\phi_{\text{rand}}$. Here, $\delta\phi_{\text{sens}}$ is defined by the argument of the integral in Eq. (4), while the integral itself takes the average value of $\delta\phi_{\text{sens}}$ over all possible random values of ϕ_{rand}. This integral assumes that ϕ_{rand} has a uniform distribution. If it is assumed that $|\mathbf{I}_{\text{noise}}| \ll |\mathbf{I}_{\text{signal}}|$, then the arctangent function can be approximated by the value of its argument. The integral in Eq. (4) then simplifies to the mean value of the sine function over a quarter period, yielding:

$$\delta\phi_{\text{sens}}=\frac{2}{\pi}\left[\frac{1}{\text{SNR}(S_0,R_n,f_{\text{ascan}})}\right]^{1/2}, \tag{5}$$

where SNR $(S_0,R_n,f_{\text{ascan}})$ is the SNR of the n'th reflector.

Because the phase of $\mathbf{I}(2\Delta x_n)$ is proportional to δx_n, displacements in a sample reflector can be tracked over time by tracking the phase over time. The instantaneous velocity of a reflector is given by the difference of δx_n on two successive A scans divided by the temporal sampling interval, which is equivalent to defining the instantaneous Doppler shift as the derivative of the phase with respect to time. This gives

$$\begin{aligned} v(t) &= \frac{\lambda_0}{2\cos\theta}f_{\text{dopp}} \\ &= \frac{\lambda_0}{4\pi\cos\theta}f_{\text{ascan}}[\angle\mathbf{I}(2\Delta x_n,t)-\angle\mathbf{I}(2\Delta x_n,t-f_{\text{ascan}}^{-1})]. \end{aligned} \tag{6}$$

Here, $\angle$ is the phase operator, λ_0 is the source center wavelength, f_{dopp} is Doppler frequency shift, and θ is the Doppler

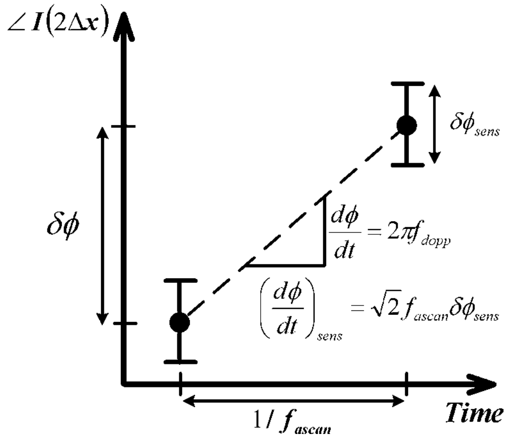

Fig. 2 Velocity sensitivity of Doppler flow imaging. Here, f_{dopp} is the Doppler frequency shift, and $\mathrm{d}\phi/\mathrm{d}t$ is experimentally calculated by taking the numerical derivative of the phase with respect to time.

angle between the optical axis and the direction of motion. The phase error in $v(t)$ is $\sqrt{2}$ times higher than the phase error in $\angle\mathbf{I}(2\Delta x_n, t_0)$. The factor of $\sqrt{2}$ arises because velocity is proportional to the numerical difference between two successive phase measurements. As such, the uncertainty in difference (i.e., velocity) must be larger than the individual data points in the difference (i.e., phase). We assume that the summation of N random data points with identical standard deviations (or errors) has an error that is $N^{1/2}$ times larger that the error of each data point. The velocity sensitivity is thus (Fig. 2):

$$v_{\text{sens}} = \frac{\lambda_0}{2\sqrt{2}\pi\cos\theta}\delta\phi_{\text{sens}} f_{\text{ascan}} = \frac{\lambda_0 f_{\text{ascan}}}{\sqrt{2}\pi^2\cos\theta(\text{SNR}(S_0, R_n, f_{\text{ascan}}))^{1/2}}. \tag{7}$$

Equation (7) is consistent with the Cramer-Rao lower bound for a model-based velocity estimator,[20] which has been previously verified[21] in TD OCT. In Doppler OCT imaging it has been suggested that the minimum observable Doppler shift is related to the inverse of the observation period, which yields a velocity sensitivity[22,23] of $\lambda_0 f_{\text{ascan}}/2$. The basis for this Fourier-limited assumption is that at least one cycle of the Doppler-induced electronic beat frequency must be sampled to detect the motion of a reflector. If we define the instantaneous Doppler shift (or velocity) as being the derivative of the phase (or position), it is clear the Fourier limit is overly restrictive. For example, if a reflector is moving at a constant velocity, the phase of the interoferometric signal increases linearly over time. The accuracy of the phase difference between two sequential points, which is directly proportional to the instantaneous Doppler shift, is limited only by the phase noise on each individual point (Fig. 2). In this light, there is no obvious requirement to sample an entire fringe of the Doppler-induced electronic beat frequency in the detector photocurrent.

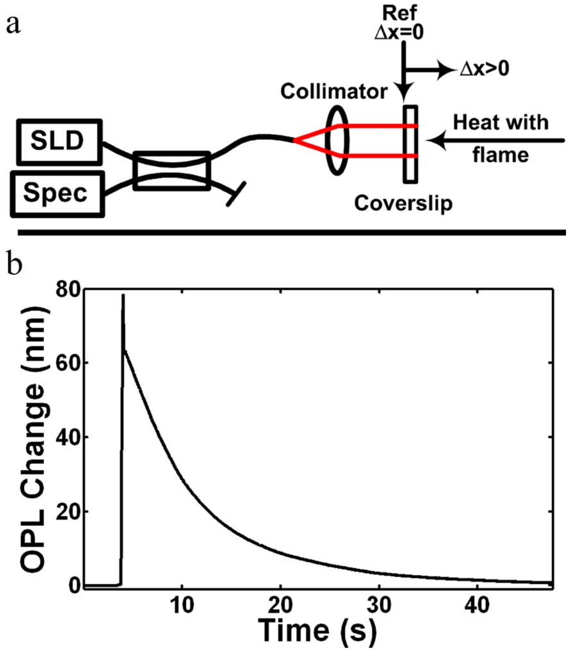

Fig. 3 (a) SDPM interferometer used for measuring thermal expansion of boroslilcate glass. The coverslip surface proximal to the interferometer generates the reference reflection. All reflections distal to this reference surface have positive displacements (i.e., $\Delta x > 0$). (b) Thermal expansion and contraction of a glass coverslip. The upswing corresponds to the application of a flame to the coverslip, and the downswing corresponds to cooling down to room temperature. The inset highlights the expansion of the coverslip.

3 Verification of Doppler Sensitivity Prediction

The major result in the previous section is that the velocity sensitivity in SD Doppler imaging is limited by the phase stability of the x domain signal, according to Eq. (7). To test this prediction, we used SDPM to measure the velocity of thermal expansion of an uncoated glass coverslip transiently heated by a butane flame. A spectral domain interferometer was constructed per Fig. 3(a). The source was a 5-mW superluminescent diode (SLD) with a center wavelength and a 3-dB bandwidth of 830 and 45 nm, respectively. The spectrometer (Spec) had a 5-ms integration time and a 40-Hz maximum readout rate. The coverslip surface reflection most proximal to the interferometer was used as the reference reflection. Reflectors distal to this surface were designated as having positive displacement with respect to the reference reflector (i.e., $\Delta x > 0$). Moreover, by design there are no reflectors with negative displacement $(\Delta x < 0)$. While this configuration does not resolve the complex conjugate ambiguity of spectral domain[24,25] OCT, it sidesteps the issue by forcing all sample displacements to have the same sign. The change in the optical path length (OPL) of the coverslip during heating and cooling was tracked by recording the phase of the x domain interference signal at a depth corresponding to the thickness of the coverslip. This phase was converted to OPL by multiplication by the quantity $\lambda_0/(4\pi n)$, where n was assumed as the index of the coverslip.

The rapid expansion and slow contraction of the coverslip is shown in Fig. 3(b). The baseline phase stability of the interference signal immediately before placing the flame near

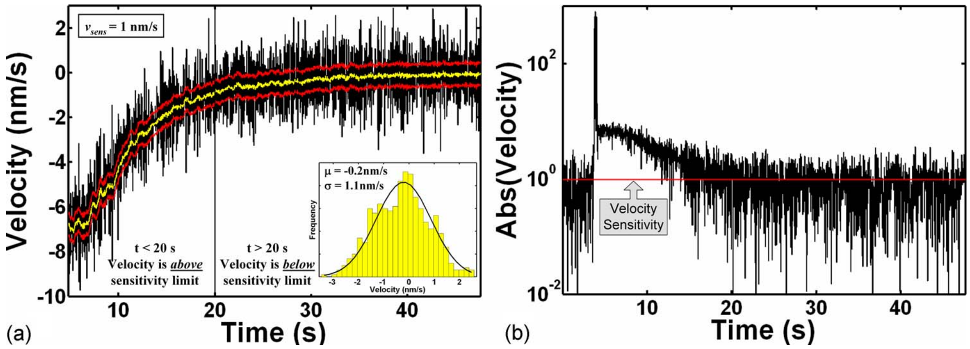

Fig. 4 (a) Velocity of thermal contraction of glass coverslip (t=4.8 to 48 s). The black curve is generated by taking the numerical derivative of the data in (b). The yellow (inner) line is the velocity estimated by lowpass filtering the raw data in black. The red (outer) lines are the velocity estimate plus/minus one-half of the predicted velocity sensitivity of 1 nm/s. The inset shows a histogram [yellow (gray) bars] of the velocity values measured for $t>20$ s. The mean (μ) and standard deviation (σ) of the measured data are shown. The black curve is a Gaussian distribution with the measured μ and σ. (b) Absolute value of the velocity of expansion and contraction calculated from (a) and plotted on a log scale.

the coverslip was 0.4 mrad (18 pm). The phase stability is defined as the standard deviation of the x domain interference phase at the depth corresponding to the coverslip thickness. The instantaneous velocity of expansion and contraction was calculated by numerically differentiating the OPL on sequential successive A scans and multiplying that quantity by the line rate [Eq. (6)].

Figure 4(a) shows the instantaneously calculated velocity while the coverslip cooled off after flame removal. The yellow curve is a smoothed estimate of the actual velocity generated by low pass filtering the phase data before calculation of the Doppler shift. The red curves represent the estimated velocity plus/minus half of the velocity sensitivity calculated using Eq. (7). The black vertical line at t=20 s represents the approximate time at which the magnitude of the velocity fell below the sensitivity of 1 nm/s, as calculated using Eq. (7). The inset to Fig. 4(a) shows a histogram of the measured velocity values for $t>20$ s. This data distribution, which is approximately Gaussian, has a standard deviation of 1.1 nm/s, consistent with the predicted velocity sensitivity of 1 nm/s.

Figure 4(a) illustrates two points. First, the experimental velocity data were bound by a range defined by the actual velocity (estimated by lowpass filtering the velocity data) and the predicted velocity sensitivity using Eq. (7). This supports Eq. (7) as a valid expression for the noise and uncertainty in a Doppler calculation given a level of phase stability. Second, it demonstrates that the magnitude of the velocity must be greater than the velocity sensitivity to be resolved from zero velocity. In other words, when the velocity magnitude is equal to the velocity sensitivity, the "velocity SNR" is unity, rendering the velocity measurement indistinguishable from zero velocity. Figure 4(b) shows the absolute value of the expansion and contraction velocity on a log scale. The predicted velocity sensitivity is shown as a horizontal red line. This figure draws an analogy with amplitude sensitivity for OCT in that the level of the "height" of the noise floor on a log plot is determined by the measurement sensitivity.

4 Measurement of Cytoplasmic Flow Using SDPM

For *in vivo* cellular measurements, an SDPM setup was relayed into a Zeiss Axiovert 200 using a documentation port, as illustrated in Fig. 5. This setup employed the source and spectrometer described in Sec. 3. Simultaneous acquisition of SDPM and visible light microscopy video was achieved by placement of an 80/20 beamsplitter in the microscope optical path. There was thus real-time display of video and A scan data. The SDPM spot size ($1/e$ diameter) on the sample was estimated from the magnification factor of the coupler fiber core being imaged onto the sample. This factor was $(L_2/L_1)\times(\mathrm{TL}/\mathrm{OBJ})$, giving a calculated spot size of 12 μm and a calculated depth of focus of 1 mm (L_n, nth lens; TL, tube lens; OBJ, objective lens; see Fig. 5 for more detail). The ratio OBJ/TL is specified by the manufacturer as the effective or net magnification of a sample object onto the documentation port. The reflection from an uncoated CS surface proximal to the SDPM interferometer acted as the reference reflection.

Several amoebas (species *A. proteus*) were placed on the other CS surface in a springwater solution. The amoeba *A. proteus* moves by extruding a pseudopod along the CS surface, and cytoplasm flows within the pseudopod along the

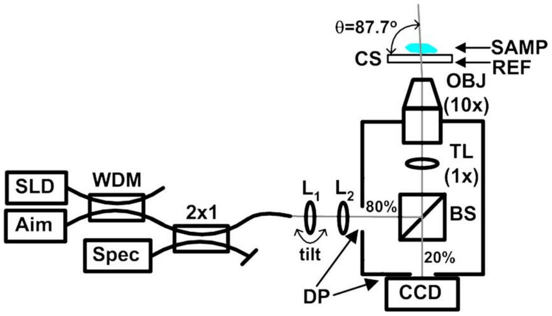

Fig. 5 SDPM setup adapted to Zeiss Axiovert 200 inverted microscope with simultaneous acquisition of SDPM and video light microscopy. A 635-nm aiming beam (Aim) is combined with an 840-nm SLD (50-nm FWHM bandwidth) with a wavelength-division multiplexing (WDM) fiber coupler. The combined light enters a 2×1 50/50 fiber coupler whose output fiber core is imaged via lenses (L) 1 and 2 onto a documentation port (DP) of the microscope with a magnification of $L_2/L_1=22$. The image formed at the documentation port is then relayed onto the sample (SAMP) with magnification of 1/10. The sample also is imaged onto a documentation port CCD. CS, coverslip; OBJ, microscope objective; REF, reference reflection; Spec, spectrometer; TL, tube lens.

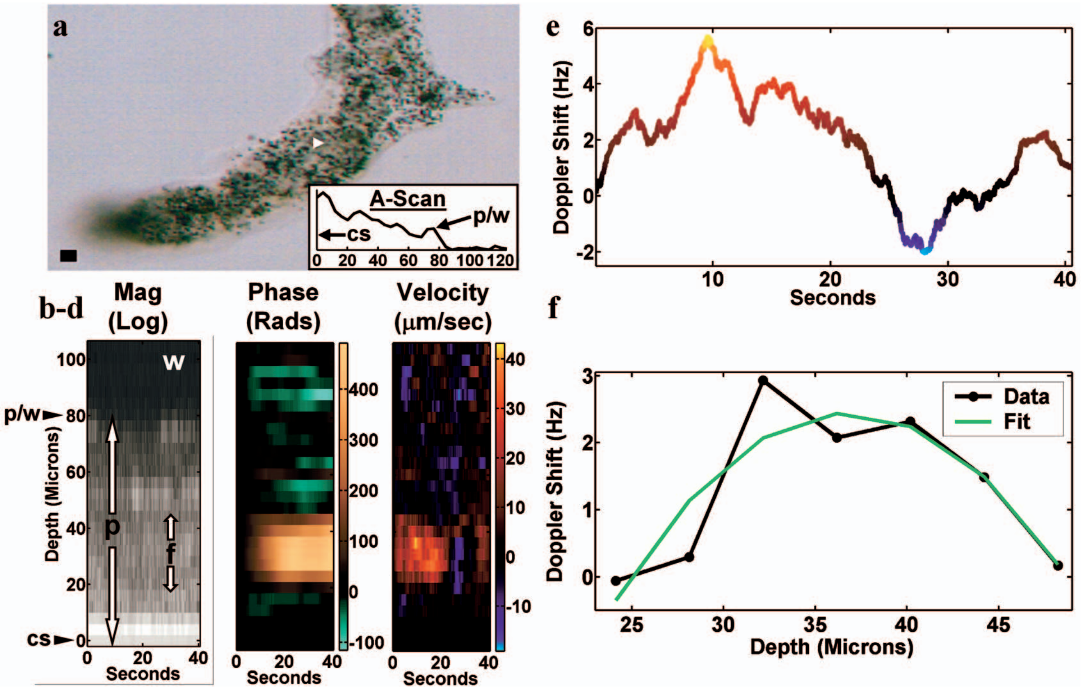

Fig. 6 (a) Photomicrograph of *A. proteus* pseudopod (p). The white triangle marks location of data collection, and black box in lower left is 10 ×10 μm. The inset to (a) shows an A scan of the pseudopod (abscissa has units of depth in micrometers, ordinate has units of reflectivity in decibels). The coverslip (cs) on which the pseudopod sits is located at zero displacement. The pseudopod/water (p/w) interface is clearly identified near 80 μm by a reflectivity peak followed by the decreased reflectivity of water. (b) M-mode magnitude image of *A. proteus* pseudopod. (c) and (d) are M-mode phase and Doppler images, respectively. The arrows marked with "f" in (b) demarcate the flowing portion of the cytoplasm as determined from the phase and Doppler data in (c) and (d), respectively. (e) Doppler shift versus time at a depth of 36 μm. (f) Doppler shift versus depth at t=20s. The green line is a least-squares parabolic fit of the flow profile (R^2=80%).

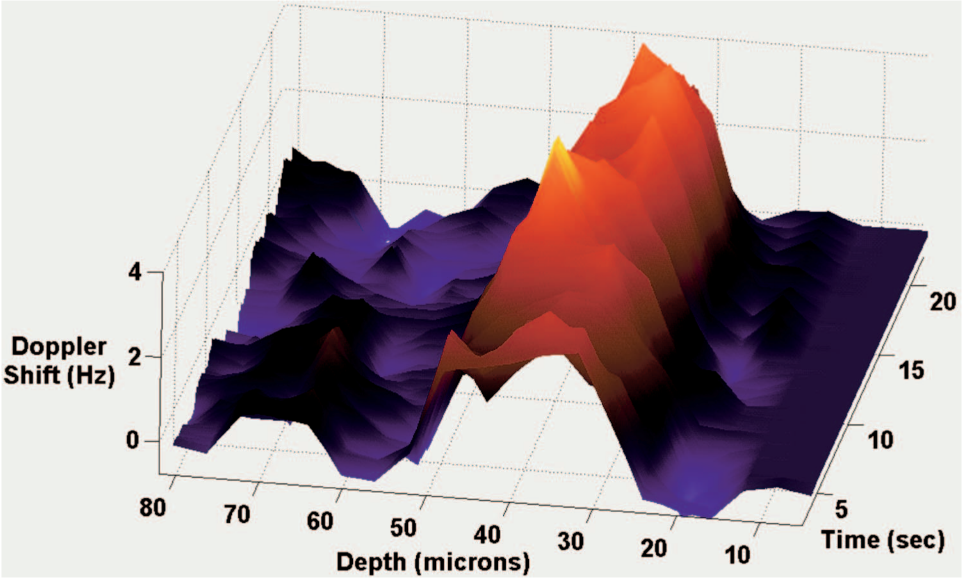

Fig. 7 Surface plot of flow-induced Doppler shift as a function of time and depth. Laminar (parabolic) cytoplasmic flow is suggested.

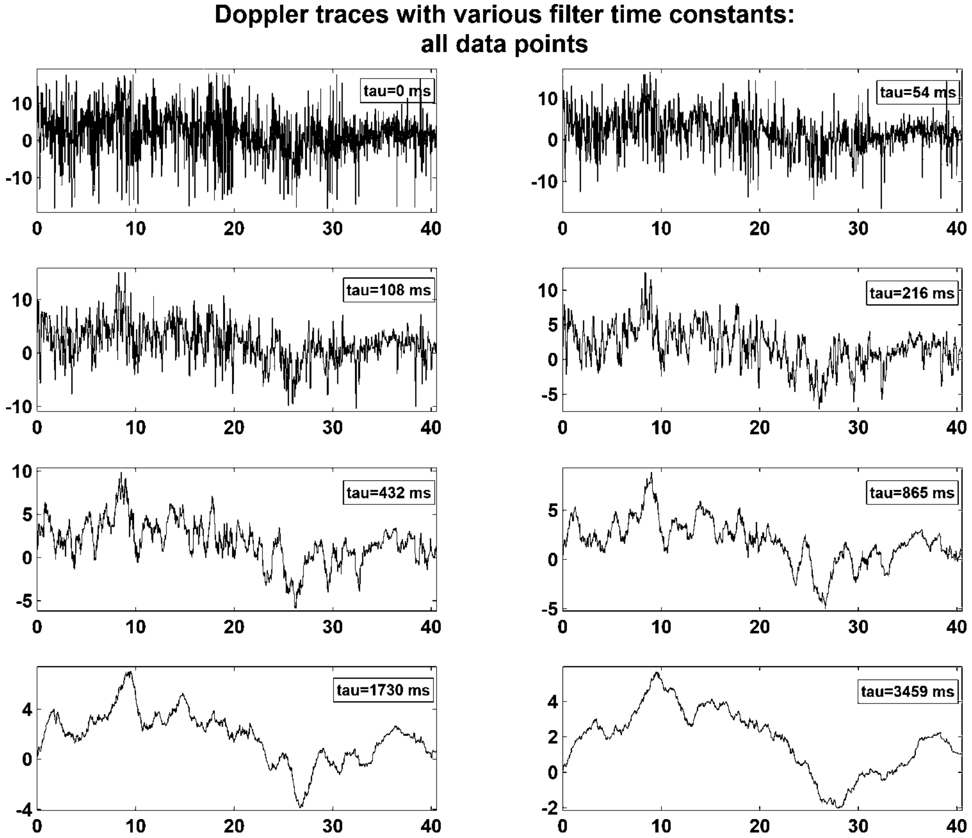

Fig. 8 Doppler shift versus time at a depth of 36 μm after processing with moving-average filters of various time constants (tau). All data points in the recording are shown. Abscissa has units of time in seconds; ordinate, Doppler shift in hertz.

direction of motion. Since this cytoplasmic streaming is nominally parallel to the coverslip surface, lens 1 (L_1) was tilted to make a Doppler angle of $\theta=87.7$ deg between the SDPM light and the streaming. This Doppler angle represents a compromise between recoupling efficiency of the reference beam (highest at 90 deg) and optimal Doppler angle (optimal at 0 deg). The angle was verified through image analysis of the position of the aiming beam on the video image taken at calibrated displacements of the objective lens along the optical axis. With respect to recoupling efficiency of the reference beam, note that standard OCT sensitivity expressions here and in the literature are typically independent of reference arm power provided that (1) reference power is much greater than sample power and (2) the system operates in the shot noise limit.

A visible light microscopic image selected from a video recording of an extruding *A. proteus* is in Fig. 6. SDPM data were recorded from the location marked with the white triangle. This location was identified with a 635-nm aiming beam that was turned off after the acquisition window was marked with the triangle. The aiming beam was turned off to avoid contamination of the data by photophobic reflex in *A. proteus*. M-mode recordings (repeated recordings at a given spatial location) of magnitude, phase, and derived Doppler images are shown in Fig. 6(b). M-mode images have a vertical axis with units of depth, a horizontal axis with units of time, and image intensity proportional to the measurement of interest (e.g., reflectivity, velocity). The Doppler map was calculated using Eq. (6) after lowpass filtering of the phase data. Between $t=18$ and 20 s, several drops of a 50-mM $CaCl_2$ solution were added to the springwater solution. This triggered a slowdown and subsequent reversal in the cytoplasmic flow. The flow reversal is manifest as a decrease in accumulated phase [Fig. 6(c)] and as a change in the sign of the Doppler shift [Figs. 6(d) and 6(e)]. The flow reversed again at $t\approx 35$ s. Overall, measured flow rates were consistent with previously reported[13] values for *A. proteus*.

Lowpass filtering of the Doppler data was performed to mitigate the influence of SNR variations due to speckle on the calculation of Doppler shift. Since speckle is multiplicative noise imposed on $\mathbf{I}(2\Delta x)$ [i.e., $\mathbf{I}=\mathbf{I}_{\text{speckle}}\times(\mathbf{I}_{\text{signal}}+\mathbf{I}_{\text{noise}})$], SNR $(S_0,R_{n2},f_{\text{ascan}})$ is modulated by this multiplicative noise as well. Additionally, the "nulls" of the speckle pattern have a phase SNR of zero since there is zero signal. These nulls give the false impression that there is zero flow in an otherwise flowing sample. Likewise, SNR is maximum at the "peaks" of the speckle pattern, and the Doppler shift at these peaks presumably will most accurately represent the sample flow velocity. The Doppler data in Figs. 6 and 7 were lowpass filtered with a moving average filter with a time constant (or width) of 3459 ms. This relatively longer time constant was chosen to emphasize changes in flow over the course of a few seconds. Figures 8 and 9 show the Doppler shift recorded at a depth of 36 μm that was lowpass filterd with time constant ranging from 0 to 3459 ms. The Doppler data is clearly interpretable

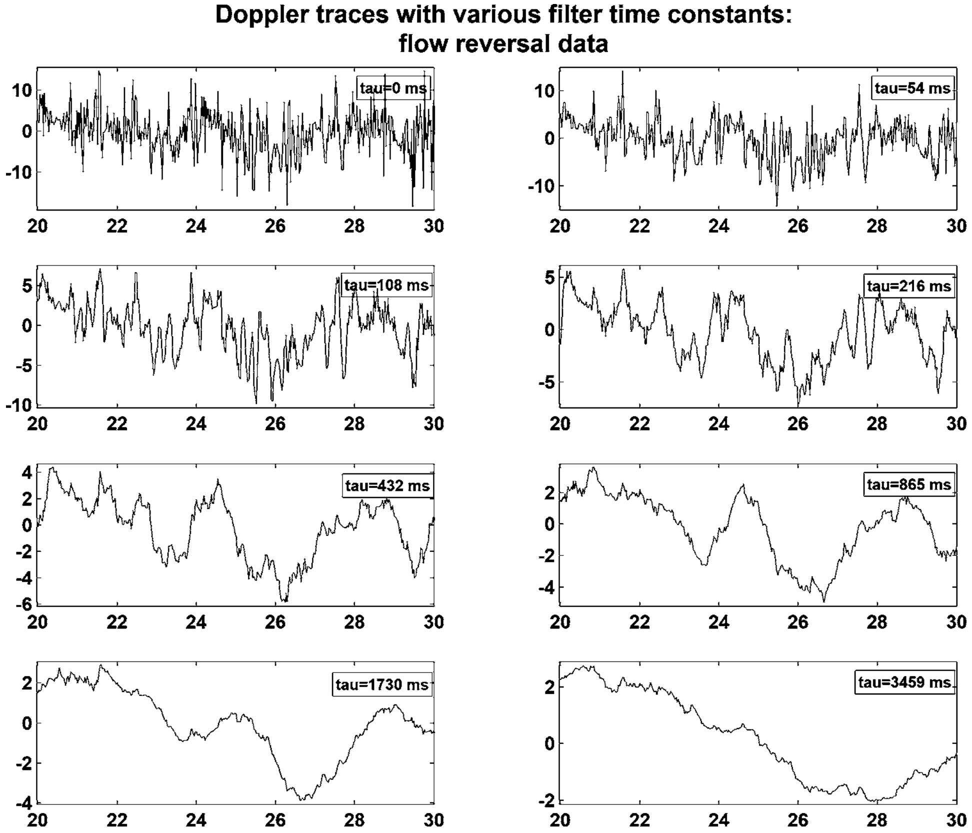

Fig. 9 Doppler shift versus time at a depth of 36 μm after processing with moving-average filters of various time constants (tau). Data points corresponding to flow reversal that occurs between 20 and 30 s are shown. Abscissa has units of time in seconds; ordinate, Doppler shift in hertz.

with little to no filtering. Figure 8 shows the entire time trace, while Fig. 9 focuses on $t=20$ to 30 s when the initial flow reversal occurred.

Visual inspection of the extruding *A. proteus* pseudopod on light microscopy indicates that the cytoplasm flows within a channel delinated on either side by nonflowing cytoplasm (the so-called “gel,” in contrast to the flowing “sol”). The gel has high viscosity and acts as a stationary conduit, while the sol, which has much lower viscosity, flows within that conduit. Flow is generated by active (i.e., adenosine triphosphate (ATP)-dependent) cytoskeletal and cytoplasmic processes. In the absence of turbulence, which would be difficult to generate owing to the viscosity of cytoplasm, the amplitude of the flow is expected to follow a parabolic profile as a function of depth. Figure 6(f), which shows the Doppler frequency as a function of depth at $t=20$ s, supports this laminar flow hypothesis. This measured flow profile matches that of an ideal parabolic flow profile with an R^2 value of 80%. The laminar flow profile also is suggested from the plot of the flow-induced Doppler shift against both depth and time in a 3-D surface plot (Fig. 7).

5 Discussion and Conclusions

Common-path interferometry has been a subject of recent interest in OCT. This interest is in part driven by the design considerations of common-path interferometry, especially since it does away with the need to pathlength-match the reference and sample arms. Common-path configurations have been proposed and demonstrated for both time domain OCT systems (see, for example, Ref. 26) and spectral domain OCT systems (see, for example, Refs. 10–12). TD common-path interferometers have similar topologies to their spectral domain counterparts, except that the spectral content of the interferometric signal is obtained using a TD autocorrelator as opposed to a SD spectrometer. While the phase stability of these TD systems has yet to be demonstrated, their phase stability is limited by the moving parts in the autocorrelator, just as the phase stability in Michelson-type TD OCT interferometers is limited by the linearity and repeatability of the reference arm group and phase delay. As such, SD common-path interferometry would be expected to have a higher level of phase stability. Additionally, since phase sensitivity is a function of amplitude sensitivity, the amplitude sensitivity advantage of SD OCT translates into a phase sensitivity advantage as well.

Phase-sensitive interferometry has the attractive ability to detect subwavelength motions of reflectors. When combined with broadband coherence interferometry, depth-indexed displacement and flow information can be obtained. As we demonstrated, the phase stability afforded by common-path SD OCT enables the acquisition of Doppler flow profiles of cytoplasmic streaming in an individual cell. This raises the exciting prospect of using SDPM to study cytoplasmic flow in a variety of cellular processes, including the development of neuronal polarity,[27] cell migration,[28] and *a-p* axis formation in embryos.[29] The use of recently developed ultra-high-resolution sources[30] and OCT imaging engines[31–33] in SDPM will enable highly detailed cross-sectional flow maps in individual eukaryotic cells.

Acknowledgments

The authors would like to thank David Choma for fruitful discussions. This work was supported by National Institute of Health (NIH) Grants R24-EB00243 and R21 RR019769.

References

1. J. A. Izatt, M. D. Kulkarni, S. Yazdanfar, J. K. Barton, and A. J. Welch, "In vivo bidirectional color Doppler flow imaging of picoliter blood volumes using optical coherence tomography," *Opt. Lett.* **22**(18), 1439–1441 (1997).
2. Z. P. Chen, T. E. Milner, D. Dave, and J. S. Nelson, "Optical Doppler tomographic imaging of fluid flow velocity in highly scattering media," *Opt. Lett.* **22**(1), 64–66 (1997).
3. B. R. White, M. C. Pierce, N. Nassif, B. Cense, B. H. Park, G. J. Tearney, B. E. Bouma, T. C. Chen, and J. F. de Boer, "In vivo dynamic human retinal blood flow imaging using ultra-high-speed spectral domain optical Doppler tomography," *Opt. Express* **11**(25), 3490–3497 (2003).
4. C. K. Hitzenberger and A. F. Fercher. "Differential phase contrast in optical coherence tomography," *Opt. Lett.* **24**(9), 622–624 (1999).
5. M. Sticker, M. Pircher, E. Gotzinger, H. Stattmann, A. F. Fercher, and C. K. Hitzenberger, "En face imaging of single cell layers by differential phase-contrast optical coherence microscopy," *Opt. Lett.* **27**(13), 1126–1128 (2002).
6. D. P. Davé and T. E. Milner, "Optical low-coherence reflectometer for differential phase measurement," *Opt. Lett.* **25**(4), 227–229 (2000).
7. T. Akkin, D. P. Davé, T. E. Milner, and H. G. Rylander, "Detection of neural activity using phase-sensitive low-coherence reflectometry," *Opt. Express* **12**(11), 2377–2386 (2004).
8. C. Yang, A. Wax, M. S. Hahn, K. Badizadegan, R. R. Dasari, and M. S. Feld, "Phase-referenced interferometer with subwavelength and subhertz sensitivity applied to the study of cell membrane dynamics," *Opt. Lett.* **26**(16), 1271–1273 (2001).
9. C. Fang-Yen, M. C. Chu, H. S. Seung, R. R. Dasari, and M. S. Feld, "Noncontact measurement of nerve displacement during action potential with dual-beam low-coherence interferometer," *Opt. Lett.* **29**(17), 2028–2030 (2004).
10. A. F. Fercher, C. K. Hitzenberger, G. Kamp, and S. Y. Elzaiat, "Measurement of intraocular distances by backscattering spectral interferometry," *Opt. Commun.* **117**(1–2), 43–48 (1995).
11. A. B. Vakhtin, D. J. Kane, W. R. Wood, and K. A. Peterson, "Common-path interferometer for frequency-domain optical coherence tomography," *Appl. Opt.* **42**(34), 6953–6958 (2003).
12. M. A. Choma, A. K. Ellerbee, C. H. Yang, T. L. Creazzo, and J. A. Izatt, "Spectral-domain phase microscopy," *Opt. Lett.* **30**(10), 1162–1164 (2005).
13. R. D. Allen, "Biophysical Aspects of Pseudopodia," in *The Biology of Amoeba*, K. W. Jeon, Ed., Academic Press, New York (1973).
14. D. L. Taylor, Y. Wang, and J. M. Heiple, "Contractile basis of ameboid movement VII. The distribution of fluorescently labeled actin in living amebas," *J. Cell Biol.* **86**(2), 590–598 (1980).
15. L. W. Janson and D. L. Taylor, "In vitro models of tail contraction and cytoplasmic streaming in amoeboid cells," *J. Cell Biol.* **123**(2), 345–355 (1993).
16. S. W. Oh and K. W. Jeon, "Characterization of myosin heavy chain and its gene in amoeba proteus," *J. Eukaryot Microbiol.* **45**(6), 600–605 (1998).
17. H. Miyoshi, Y. Kagawa, and Y. Tsuchiya, "Chaotic behavior in the locomotion of amoeba proteus," *Protoplasma* **216**(1–2), 66–70 (2001).
18. M. Dominik, W. Klopocka, P. Pomorski, E. Kocik, and M. J. Redowicz, "Characterization of amoeba proteus myosin VI immunoanalog," *Cell Motil. Cytoskeleton* **61**(3), 172–188 (2005).
19. M. A. Choma, M. V. Sarunic, C. Yang, and J. A. Izatt, "Sensitivity advantage of swept-source and Fourier-domain optical coherence tomography," *Opt. Express* **11**(18), 2183–2189 (2003).
20. H. L. V. Trees, *Detection, Estimation, and Modulation Theory*, Pt. 1, Wiley, New York (1968).
21. S. Yazdanfar, C. Yang, M. V. Sarunic, and J. A. Izatt, "Frequency estimation precision in Doppler optical coherence tomography using the Cramer-Rao lower bound," *Opt. Express* **13**(2), 410–416 (2005).
22. M. D. Kulkarni, T. G. van Leeuwen, S. Yazdanfar, and J. A. Izatt, "Velocity-estimation accuracy and frame-rate limitations in color Doppler optical coherence tomography," *Opt. Lett.* **23**(13), 1057–1059 (1998).
23. Y. H. Zhao, Z. P. Chen, C. Saxer, S. H. Xiang, J. F. de Boer, and J. S. Nelson, "Phase-resolved optical coherence tomography and optical Doppler tomography for imaging blood flow in human skin with fast scanning speed and high velocity sensitivity," *Opt. Lett.* **25**(2), 114–116 (2000).
24. M. Wojtkowski, A. Kowalczyk, R. Leitgeb, and A. F. Fercher, "Full range complex spectral optical coherence tomography technique in eye imaging," *Opt. Lett.* **27**(16), 1415–1417 (2002).
25. M. V. Sarunic, M. A. Choma, C. H. Yang, and J. A. Izatt, "Instantaneous complex conjugate resolved spectral domain and swept-source OCT using 3×3 fiber couplers," *Opt. Express* **13**(3), 957–967 (2005).
26. F. Feldchtein, J. Bush, G. Gelikonov, V. Gelikonov, and S. Piyevsky, "Cost effective, all-fiber autocorrelator based 1300 nm OCT system," in *Coherence Domain Optical Methods and Optical Coherence Tomography in Biomedicine IX*, *Proc. SPIE* **5690**, 349–355 (2005).
27. F. Bradke and C. G. Dotti, "Neuronal polarity: vectorial cytoplasmic flow precedes axon formation," *Neuron* **19**(6), 1175–1186 (1997).
28. A. J. Ridley, M. A. Schwartz, K. Burridge, R. A. Firtel, M. H. Ginsberg, G. Borisy, J. T. Parsons, and A. R. Horwitz, "Cell migration: integrating signals from front to back," *Science* **302**(5651), 1704–1709 (2003).
29. S. N. Hird and J. G. White, "Cortical and cytoplasmic flow polarity in early embryonic cells of *Caenorhabditis elegans*," *J. Cell Biol.* **121**(6), 1343–1355 (1993).
30. W. Drexler, U. Morgner, F. X. Krtner, C. Pitris, S. A. Boppart, X. D. Li, E. P. Ippen, and J. G. Fujimoto, "In vivo ultrahigh-resolution optical coherence tomography," *Opt. Lett.* **24**(17), 1221–1223 (1999).
31. B. Cense, N. A. Nassif, T. C. Chen, M. C. Pierce, S-H Yun, B. H. Park, B. E. Bouma, G. J. Tearney, and J. F. de Boer, "Ultrahigh-resolution high-speed retinal imaging using spectral-domain optical coherence tomography," *Opt. Express* **12**(11), 2435–2447 (2004).
32. M. Wojtkowski, V. J. Srinivasan, T. H. Ko, J. G. Fujimoto, A. Kowalczyk, J. S. Duker, "Ultrahigh-resolution, high-speed, Fourier domain optical coherence tomography and methods for dispersion compensation," *Opt. Express* **12**(11), 2404–2422 (2004).
33. R. A. Leitgeb, W. Drexler, A. Unterhuber, B. Hermann, T. Bajraszewski, T. Le, A. Stingl, and A. F. Fercher, "Ultrahigh resolution Fourier domain optical coherence tomography," *Opt. Express* **12**(10), 2156–2165 (2004).